ADVANCED FUNCTIONAL MATERIALS
www.afm-journal.de

Reversible and Rapid Laser Actuation of Liquid Crystalline Elastomer Micropillars with Inclusion of Gold Nanoparticles

Xiyang Liu, Renbo Wei, Phong Tran Hoang, Xiaogong Wang, Tao Liu,* and Patrick Keller**

It is highly desirable for liquid crystal elastomer (LCE) based microactuators to activate and actuate in a highly controlled fashion without perturbing the surrounding environment. To reach this goal, in this study, a novel experimental protocol is developed to successfully incorporate gold nanosphere (AuNS) and gold nanorod (AuNR) into polyacrylate based LCE elastomer to fabricate LCE/AuNR and LCE/AuNS micropillars or microactuators. The effect of gold nanoparticle inclusion has been studied by spectroscopy (UV–vis-near-infrared), microscopy (transmission electron microscopy), thermal analysis (differential scanning calorimetry and thermogravimetric analysis), and x-ray scattering (wide-angle x-ray scattering and small-angle x-ray scattering). Finite element analysis is performed to examine the feasibility of utilizing the photothermal effect of AuNR/AuNS to enable photothermal actuation of LCE/AuNR and LCE/AuNS micropillars. The comparative experimental studies on the thermal and photothermal actuation behavior of the LCE, LCE/AuNS, and LCE/AuNR micropillar suggested that AuNR is an excellent candidate for developing high-performance LCE actuators with photothermal actuation capability. With inclusion of less than 1 wt% of AuNR, the very high maximum actuation strain (30%) and rapid response (a few seconds) have been achieved in LCE/AuNR micropillar actuators under 635 nm laser irradiation.

1. Introduction

Liquid crystalline elastomers (LCEs) are composed of a rubbery/elastomeric network, in which the rod, disc, or amphiphilic mesogenic moieties are attached to or incorporated into the flexible chain polymer backbones of the network.[1] This unique structure is responsible for the interplay between liquid crystal order of the mesogenic units and the entropic elasticity of the rubbery network. As a consequence, a change of the orientation order of the mesogenic units by external stimuli can result in a change of the polymer backbone conformation and therefore the macroscopic shape of LCEs.[2–5] The ability for LCE to change its shape reversibly makes it an attractive alternative to piezoelectrics, hydrogels, and dielectric elastomers in developing various novel sensing and actuating applications,[6–8] such as microactuator to mimic the motion of natural cilia,[9] light driven plastic motors,[10] and responsive smart surfaces.[11,12] Different external stimulating schemes, such as direct heating,[11,13] electric current caused heating,[14] light-induced *cis–trans* isomerization of azobenzene mesogens[9,15,16] have been attempted to trigger the shape change of LCEs. Besides the aforementioned methods, there is recently an emergence on using nanoparticles to form LCE nanocomposites or nanohybrids to activate their shape change under different external stimuli. With inclusion of carbon black (CB) nanoparticles, Chambers et al. developed electrically conductive LCE/CB nanocomposites.[17] By passing electric currents, the temperature of LCE/CB can be increased to initiate the shape change. Similar approach was taken by Yang et al.[18] and Kohlmeyer and Chen[19] to prepare LCE/SWCNT (single-walled carbon nanotubes) nanocomposites with very low SWCNT loading (0.1–0.2 wt%). Upon IR irradiation on the LCE/SWCNT composite film for a few minutes, a large and reversible deformation was demonstrated. Kaiser et al. presented a LCE composite containing iron oxide magnetic nanoparticles and demonstrated its shape contraction of 27% in minutes with AC (300 kHz) induction heating method.[20] With incorporation of gold nanospheres (AuNS) of diameter ≈2 nm into micrometer-sized cylindrical actuators, Sun et al. demonstrated local heating by a focused near-infrared (NIR) laser beam to bend a pillar microactuator reversibly.[21] Through

X. Liu, R. Wei, Prof. X. Wang
Department of Chemical Engineering
Key Laboratory of Advanced Materials (MOE)
Tsinghua University
Beijing 100084, P.R. China
E-mail: wxg-dce@mail.tsinghua.edu.cn
P. T. Hoang, Prof. T. Liu
High-Performance Materials Institute
Florida State University
2005 Levy Ave., Tallahassee, FL 32310, USA
E-mail: liutao@eng.fsu.edu
Prof. P. Keller
Institut Curie
Centre de Recherche, CNRS UMR 168
Université Pierre et Marie Curie
26 rue d'Ulm 75248 Paris CEDEX 05, France
E-mail: patrick.keller@curie.fr
Prof. P. Keller
Department of Chemistry and Biochemistry and Liquid Crystal Materials Research Center
University of Colorado
Boulder, CO 80309, USA

DOI: 10.1002/adfm.201500443

enhancing the thermal conductivity of LCE, AuNS of ≈3 nm in diameter have been shown to be able to significantly reduce the time response of the LCE shape change when heated directly.[22]

As compared to other types of nanoparticles, the unique localized surface plasmon resonance (LSPR)[23,24] and the associated LSPR enhanced photothermal effect [25–28] of gold nanoparticles (AuNP) make them especially interesting in developing multifunctional LCE/AuNP composites with remote triggering capability. First, at the resonance condition, the optical absorption cross section, C_{abs}, of AuNP is high, which facilitates better photothermal conversion efficiency and therefore can induce rapid shape-changing response for LCE/AuNP upon laser irradiation. The experimentally determined C_{abs} for AuNS with diameter of 20.6 nm[29] and gold nanorod (AuNR) with diameter of 12.4 nm and length of 42 nm[30] was reported to be 12.4×10^{-18} and 66.2×10^{-18} cm^2 per Au-atom, respectively, which is significantly higher than that of SWCNTs ($\approx 1.0 \times 10^{-18}$ cm^2 per C-atom at 785 nm).[31–33] Second, the resonant optical absorption behavior of AuNP, allows for the development of light-responsive LCEs with wavelength-selective capability. This is particularly true for AuNR, since its longitudinal LSPR can be readily adjusted via synthetically tailoring the aspect ratio.[34,35] The wavelength-selectivity cannot be implemented through forming LCE/CB, LCE/SWCNT, and LCE/iron oxide nanocomposites as reported previously,[17–20] since all these nanoparticles show broadband absorption characteristics. Finally, as compared to SWCNT and iron oxide, the very low optical quantum yield of AuNPs imparts them a near 100% photothermal conversion efficiency.[36,37] The earlier work by Xiao et al. has reported the inclusion of AuNR in shape memory polymer (SMP)—polyurethanes to implement laser-induced rapid shape change.[38] Nevertheless, the nonreversibility of the shape change in SMP/AuNR has been a major drawback of this system. In this study, we reported the first-of-a-kind study on the synthesis and fabrication of AuNS and AuNR enabled LCE micropillars and their photothermal actuation behavior upon visible laser irradiation. In contrast to the previously reported SMP/AuNR nanocomposite, the LCE/AuNP micropillars can be rapidly and reversibly actuated by a visible laser irradiation with large strain response. As such, one can overcome the difficulties of direct heating scheme used in previous work for actuating micropillars,[11,13,39] which are energy inefficient and highly undesirable in operating microactuator devices. Considering the great interest in the development of LCE based micro and nanoactuators,[39–44] we expect the new approach presented in this work can be a viable avenue to enable high-performance LCE-based micro and nanoactuating technologies.

2. Results and Discussion

2.1. Fabrication and Characterization of LCE, LCE/AuNR, and LCE/AuNS Micropillars

As described in the Experimental Section, the nanoparticles of AuNR and AuNS were synthesized by following the seed-mediated growth method.[45] The formation of AuNR and AuNS was confirmed by the UV–vis–NIR spectroscopy and transmission electron microscopy (TEM) imaging. The UV–vis–NIR spectra of the as-synthesized AuNR and AuNS aqueous dispersion were shown in **Figure 1**. The absorption spectrum of AuNR (Figure 1a) is signified by the two salient absorption bands. One is located at 532 nm and the other is located at 670 nm. These two absorption features are, respectively, attributed to the transverse and longitudinal surface plasmon resonance of AuNR. In contrast to AuNR, the AuNS only shows one LSPR band located at 520 nm (Figure 1d). The shapes of AuNR and AuNS were also confirmed by TEM imaging. The results are, respectively, shown in Figure 1b,e. According to TEM, the aspect ratio of the AuNR was estimated to be ≈2.5; and the diameter of AuNS was determined as ≈15 nm in average.

Previous study on the seed-mediated growth of AuNR found that ≈15% of the initial gold supply could be finally reduced to form nanorods.[30] With this conversion rate and using the absorbance value at the longitudinal resonance (670 nm) of AuNR dispersion, we estimated the optical absorption cross section or extinction coefficient, C_{abs}, of AuNR according to Lambert–Beer's law. The result is $C_{abs} = 5.52 \times 10^{-18}$ cm^2 per Au-atom. For AuNR of similar aspect ratio and size, Orendorff and Murphy reported a value of $C_{abs} = 5.32 \times 10^{-18}$ cm^2 per Au-atom,[30] which agrees with our result. The optical absorption cross section of AuNS $C_{abs} = 2.27 \times 10^{-18}$ cm^2 per Au-atom was similarly determined at the resonance wavelength (520 nm). It also agrees well with that of $C_{abs} = 2.16 \times 10^{-18}$ cm^2 per Au-atom reported previously.[33]

To prepare LCE/AuNR and LCE/AuNS composites, the as-prepared AuNR and AuNS aqueous dispersions were first subjected to repeating centrifugation and washing treatment to remove the surfactant molecules (cetyltrimethyl ammonium bromide (CTAB)). After centrifugation and washing process, an appropriate amount of AuNR or AuNS precipitates were then redispersed in the solution of LCE monomer (4″-acryloyloxybutyl 2,5-di(4′-butyloxybenzoyloxy) benzoate (4-ADBB)) in tetrahydrofuran (THF) to form 4-ADBB/AuNR or 4-ADBB/AuNR composite dispersion with the gold concentration controlled at 1 wt% relative to the LCE monomers. Subsequent to evaporation of THF, the 4-ADBB/AuNR and 4-ADBB/AuNS were then UV-cured by following the procedures detailed in the Experimental Section to form LCE/AuNR and LCE/AuNS composite films or micropillar arrays. Thermogravimetric analysis (TGA) was performed to confirm the mass concentration of AuNR and AuNS in the finally formed LCE/AuNR and LCE/AuNS composite samples. In the former case, the TGA resulted in a 1.18 wt% gold loading; and in the latter case, the TGA gave a gold loading of 1.07 wt%. The results of mass loss with temperature for LCE, LCE/AuNR, and LCE/AuNS can be found in Figure S1, Supporting Information.

The dispersion states of AuNR and AuNS in the LCE matrix were examined by UV–vis–NIR spectroscopy and TEM imaging. The UV–vis–NIR spectra of LCE/AuNR and LCE/AuNS composite film are shown, respectively, in Figure 1a,d. In the same wavelength range (400–1000 nm), the neat LCE thin film shows no absorption features (Figure S2, Supporting Information). As noted in Figure 1a,d, in comparison with that of AuNR and AuNS aqueous dispersion, the LSPR bands of both AuNR and AuNS in LCE matrix show red-shift and broadening effect. This is due to the different dielectric environment of AuNP in LCE matrix and aqueous dispersion.[38] In addition, the composite

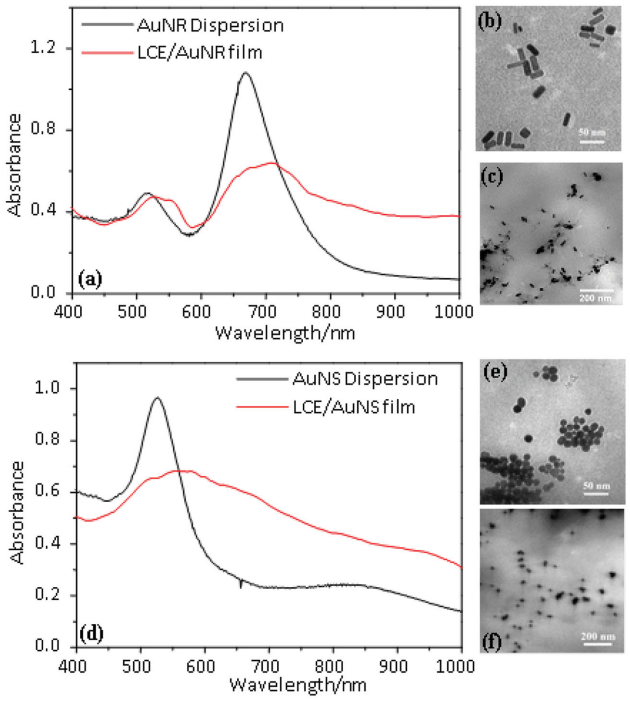

Figure 1. a) Comparison of the UV–vis–NIR spectra of AuNR in the as-synthesized aqueous dispersion and LCE/AuNR (1 wt%) composite film; b) TEM image of the as-synthesized AuNR; c) TEM image of AuNR aggregation states in ultrathin sectioning (100 nm) of LCE/AuNR (1 wt%) composite thin film; d) comparison of the UV–vis–NIR spectra of AuNS in the as-synthesized aqueous dispersion and LCE/AuNS (1 wt%) composite film; e) TEM image of the as-synthesized AuNS; f) TEM image of AuNS aggregation states in ultrathin sectioning (100 nm) of LCE/AuNS (1 wt%) composite thin film.

film preparation process may induce AuNP aggregation, which could also cause the broadening of LSPR bands. Ultrathin sectioning (100 nm in thickness) was applied to both the LCE/AuNR and LCE/AuNS composite films to further examine the dispersion states of AuNP by TEM imaging. The results are shown in Figure 1c,f, where the sparsely dispersed and slightly aggregated AuNR and AuNS particulate structures can be clearly seen.

Given the slight aggregation issue, the inclusion of low concentration of AuNP in LCE matrix has not adversely affected its capability for forming micropillars in silicone mold. This point can be seen in **Figure 2**, where, as representative examples, the optical microscopic images of micropillar arrays made from LCE/AuNR composite and neat LCE are compared. Shown in the insets of Figure 2a,b are the isolated LCE and LCE/AuNR pillars suspended in silicone oil. The length and diameter of the pillars in both cases are ≈70 and 25 μm, respectively. The optical images shown in Figure 2 suggest that, in terms of pillar shape and size, the macroscopic integrity of the micropillars formed by LCE/AuNP is not qualitatively different from that made from neat LCE polymers. Moreover, in consistent with the earlier findings,[13] when viewed under crossed polarizer and analyzer configuration, both the LCE and LCE/AuNP pillars show optical birefringence with the optical axis pointing along the pillar axis direction.

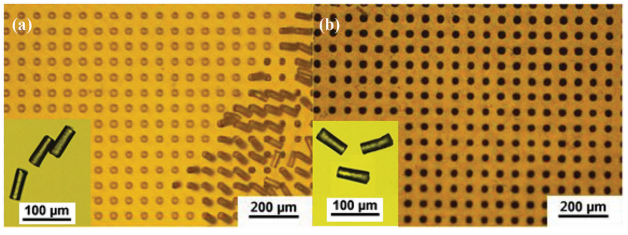

Figure 2. a) Optical image of the LCE micropillar arrays. Inset shows the isolated LCE pillars manually cut from the array by a blade; b) optical image of the LCE/AuNR (1 wt%) micropillar arrays. Inset shows the isolated LCE/AuNR pillars manually cut from the array by a blade.

The nematic–isotropic phase transition of the mesogenic units in LCE is responsible for the reversible macroscopic shape changing behavior of LCE polymers. To examine the effect of inclusion of AuNP on this important issue, differential scanning calorimetry (DSC) was performed to compare the behavior of heat flow with temperature for LCE, LCE/AuNR (1 wt%), and LCE/AuNS (1 wt%). The results are shown in **Figure 3**a. The DSC results indicate that the LCE, LCE/AuNS, and LCE/AuNR have a similar nematic–isotropic phase transition temperature (T_{NI}) at 100 °C. Moreover, the heat flow per unit mass induced by nematic–isotropic phase transition in LCE polymer and LCE/AuNS is comparable, but significantly smaller than that in LCE/AuNR composite. The greatly enhanced heat flow in LCE/AuNR can be explained as that the presence of AuNR is able to increase the ordered structures of the mesogenic units of the LCE host polymer. This order-enhancement ability of AuNR has been reported in a previous work by Liu et al.,[46] where they demonstrated that, due to the liquid crystal elasticity-mediated interaction between AuNR and LC molecules, the AuNR could form large-scale and self-aligned assemblies in nematic liquid crystals. To confirm the order-enhancement ability of AuNR in LCE, wide-angle and small-angle x-ray scattering measurements (WAXS and SAXS) were performed for LCE, LCE/AuNS, and LCE/AuNR. Figure 3b,c, respectively, shows the acquired WAXS and SAXS scattering intensity patterns. Clearly, all these samples show almost identical WAXS scattering pattern (Figure 3b), which suggests that, at small length scales (2θ: 5°–50°; scattering vector $\mathbf{q}$: 3.6–34.4 nm^{-1}; d-spacing = $2\pi/q$: 0.182–1.767 nm), the LCE/AuNS and LCE/AuNR composite samples show no qualitative difference on the ordered microstructures from neat LCE polymer. In contrast to WAXS, the SAXS scattering pattern of LCE/AuNR shows a silent feature at scattering vector $\mathbf{q} \approx 0.5$ nm (d-spacing ≈ 12.6 nm) that is absent in either LCE or LCE/AuNS samples. On the basis of the combined DSC, WAXS, and SAXS results shown in Figure 3, it seems evident that the order-enhancement ability of AuNR in LCE is related to the shape anisotropy of AuNR. More specifically, the alignment of LC mesogens induced by the magnetic field and/or the PDMS mold and the anisotropic interaction between AuNR and LC molecules in LCE/AuNR expects to play a critical role to facilitate the formation of large-scale ordered AuNR assemblies. As such, the LCE/AuNR demonstrated different nematic–isotropic phase transition (DSC) and microstructures (SAXS) than LCE and LCE/AuNS samples. However, to fully understand this issue, it requires an in-depth study of the physical nature and origin of the ordered structure appeared at the large-length scale in LCE/AuNR, which is out of the scope of our current work.

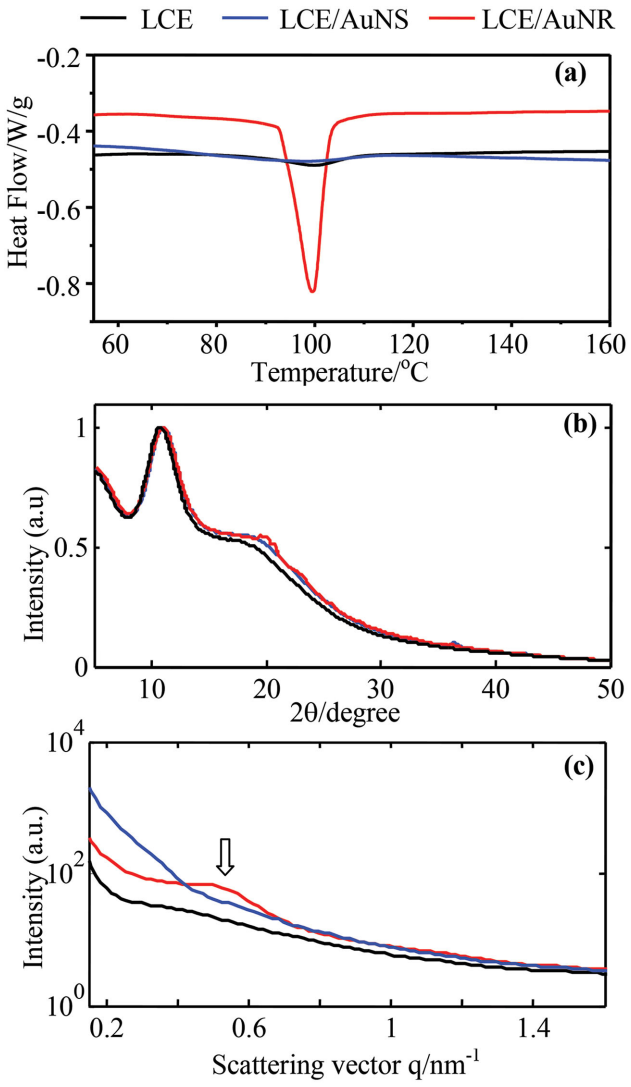

Figure 3. Effect of AuNP inclusion (1 wt%) on a) the nematic–isotropic phase transition of LCE by differential scanning calorimetry (DSC); b) microstructures of LCE polymer at small length scales by wide-angle x-ray scattering (WAXS); and c) microstructures of LCE polymer at longer length scales by small-angle x-ray scattering (SAXS).

2.2. Thermal Actuation of LCE, LCE/AuNR, and LCE/AuNS Micropillars

The reversible thermal actuation of LCE micropillars has been well-established in our previous work.[13] With increasing temperature, the pillar shrinks in length and expands in diameter. As shown by the optical images in **Figure 4**a, the three types of pillars—LCE, LCE/AuNR (1 wt%), and LCE/AuNS (1 wt%)—all clearly show the same kind of actuation behavior. When the temperature increases from 30 to 115 °C, regardless of the pillar type, the length is reduced and the diameter is increased. That the relaxed micropillar is shorter and thicker implies that, at low temperature, the director of the mesogenic units is aligned in the pillar axis direction and the polymer backbone takes a prolate shape. When the temperature increases above the nematic–isotropic phase transition, a reduction of the orientation order of the mesogenic units drives the polymer backbone from an initially anisotropic to a relaxed isotropic conformation. As such, the pillar shrinks in length and expands in diameter. By normalizing the pillar length at different temperature to that at 30 °C, Figure 4b compares in detail the length change of the isolated pillars at different temperatures. The results clearly suggest that, the onset temperature to induce an apparent length change for all three types of pillars is similar. It is ≈100 °C, which agrees with the nematic–isotropic phase transition temperature (T_{NI}) determined by DSC (Figure 3a). Moreover, in all three cases, the length of the fully relaxed pillar is ≈73% of its original length, which corresponds to a maximum actuation strain of ≈27%. The thermal actuation studies suggest that, with inclusion of a small amount of AuNP, the micropillars made from LCE/AuNR and LCE/AuNS have the same excellent thermal actuation performance as the neat LCE micropillars. Moreover, as shown next, the LCE/AuNP micropillars also possess additional functionalities in that they can be photothermally actuated with visible laser irradiation.

2.3. Photothermal Actuation of LCE, LCE/AuNR, and LCE/AuNS Micropillars

Figure 5a schematically shows a homemade/assembled setup in combination with an optical microscope for visualizing and recording the shape change of micropillars under photothermal actuation. The setup is composed of a high-power diode laser of wavelength 635 nm for photoirradiation and the mirror/lens combination for beam shaping and maneuver. The shutter in the beam path is manually operated for controlling the on-off of the photothermal actuation of the micropillars. With this setup, the maximum power density of the beam delivered to where the micropillars were located has been determined to be ≈95 W cm^{-2}. A photograph of the optical setup and the related details on the determination of the laser power density can be found in Figure S3a,b, Supporting Information. All the photothermal actuation experiments as described in the following were performed with the laser power density maintained at 95 W cm^{-2}.

Thermal actuation experiments (Figure 4) suggested that the onset temperature to actuate the LCE or LCE/AuNP micropillars is 100 °C. This means that the laser irradiation induced temperature rise has to be more than 70 °C in order to photothermally actuate the shape change of our micropillars at room temperature. We first performed finite element analysis (FEA) to check this feasibility by considering that the maximum laser power density in our photothermal actuation setup was 95 W cm^{-2}. In the FEA analysis, we simulated the temperature rise of a LCE/AuNR and LCE/AuNS micropillar immersed in silicone oil bath under varied power of laser irradiation. In the simulation, the experimentally observed pillar size was used—length L = 72.2 µm and diameter D = 24.6 µm. The specific heat (1.47 J g^{-1} K^{-1}), thermal conductivity (0.18 W m^{-1} K), and density (1.19 g cm^{-3}) of polyacrylate at room temperature were taken in our calculations for LCE/AuNP micropillar. By assuming the laser power absorbed by AuNP in the pillar is completely converted into heat, we can calculate the heat source density q (W cm^{-3}) by $q = 4P[1-\exp(-C_{abs}N_A DC\rho/M_{Au})]/\pi D = 4P[1-\exp(-\alpha D)]/\pi D$, where P is the laser power density,

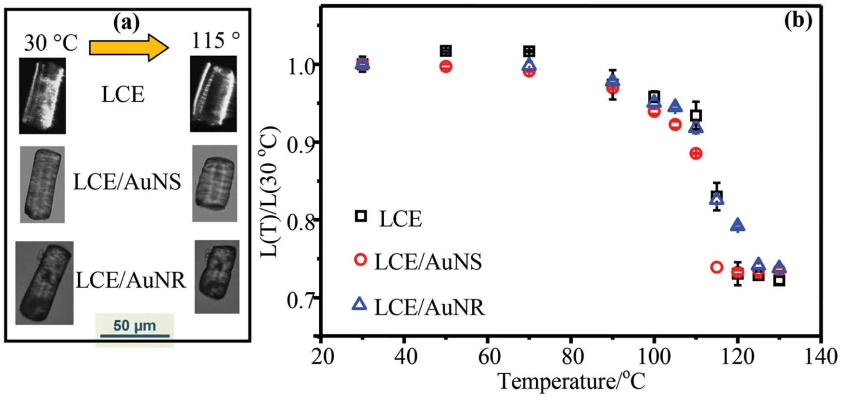

Figure 4. a) Optical images of the thermally actuated LCE, LCE/AuNS (1 wt%), and LCE/AuNR (1 wt%) micropillars at 30 and 115 °C; b) comparison of the length–temperature behavior for LCE, LCE/AuNS (1 wt%), and LCE/AuNR (1 wt%) micropillars under thermal actuation. The length is normalized by the value at 30 °C.

N_A is Avogadro's number, D is the pillar diameter, C is the mass concentration of AuNP, ρ is the pillar density, M_{Au} is the atomic mass of gold, and α is the optical absorption coefficient of the pillar. According to the experimental results obtained previously, the optical absorption cross section C_{abs} was taken as the value of 5.52×10^{-18} cm^2 per Au-atom for AuNR and 2.27×10^{-18} cm^2 per Au-atom for AuNS, respectively. The mass concentration of AuNP C was 1.0 wt%. To estimate the heat transfer coefficient h, the physical and thermal properties of silicone oil were taken from the performance test results of KF-96-350 by Shin-Etsu Chemical Co., Ltd.[47] KF-96-350 has similar physical and chemical properties as the silicone oil used in our experiments. In evaluating h, we used the empirical correlation developed by Churchill and Chu for a horizontal cylinder in free convection case.[48] The calculated value of h in the temperature range of 25–150 °C is 2414.2 ± 3.8 W m^{-2} K^{-1}. With the parameters given above, the transient heat transfer problem of a cylindrical LCE/AuNR or LCE/AuNS micropillar in silicone oil was solved by finite element method with COMSOL—a commercial multiphysics software package. Figure 5b shows the volume-averaged temperature rise for the LCE/AuNR pillar at steady-state when irradiated with different laser power density. The inset of Figure 5b also includes a representative example to show the temperature distribution of the LCE/AuNR pillar irradiated by a 95 W cm^{-2} laser. **Table 1** lists the FEA results on the temperature rise of LCE/AuNR (1 wt%) and LCE/AuNS (1 wt%) micropillar for comparison. According to the FEA simulation result, we have estimated that, in order to photothermally actuate the shape change of the LCE/AuNR (1 wt%) micropillar suspended in silicone oil at room temperature (temperature rise $\Delta T = T_{NI} - 25$ °C = 75 °C), the required laser power density should be 162.2 W cm^{-2} or higher. At 95 W cm^{-2} irradiation, the temperature rise is 44.2 °C.

The FEA results suggest that our current photothermal actuation setup is not able to deliver sufficient laser power to actuate the shape change of the LCE/AuNR micropillar at room temperature. To overcome this difficulty and demonstrate the concept, we raised the temperature of the silicone oil bath to 80 °C to perform the photothermal actuation experiments. Figure 5c shows the snapshots of the photothermal actuation of the LCE/AuNR micropillar at 80 °C. Clearly, when the laser irradiation is switched on, the LCE/AuNR micropillar immediately starts to shrink in length and expand in diameter. Upon switching off the laser irradiation, the LCE/AuNR micropillar quickly recovers to its original shape. With a quantitative frame-by-frame image analysis of the photothermal actuation video, we further examined the time-dependent actuation behavior of the LCE/AuNR (1 wt%) micropillar at 80 °C. **Figure 6**a,b, respectively, show the time-dependent length change of the LCE/AuNR micropillar in the irradiation stage and the recovery stage. Similar results for the time-dependent diameter change are also shown in Figure 6c,d. The results shown in Figure 6 clearly reveal the rapid photothermal actuation response of the LCE/AuNR micropillar. Subsequent to laser irradiation being switched on, the length contraction and diameter expansion of the pillar completed within 5 s. When the laser irradiation was switched off, the LCE/AuNR micropillar quickly expanded in length and shrank in diameter and reached its original state within less than 1.5 s. According to the thermal actuation experiments of LCE/AuNR micropillar (Figure 4), at 80 °C, the thermal actuation effect is negligible. Considering this fact, we concluded that the photothermal effect plays the key role to induce the reversible size change of the LCE/AuNR micropillar as observed in Figures 5c and 6. Certainly, the photothermal effect is a result of the inclusion of AuNR. To further strengthen this point, the photothermal actuation experiments for a neat LCE micropillar at 80 °C were also performed. Figure S4, Supporting Information, summarizes the length and diameter values of the LCE micropillar in the irradiation and recovery stage. As expected, there is no apparent size change observed for the LCE micropillar in both stages.

To compare the thermal and photothermal actuation behavior of the micropillars and investigate the shape effect of gold nanoparticles (AuNR vs AuNS), we performed thermal and photothermal actuation experiments for LCE, LCE/AuNR (1 wt%), and LCE/AuNS (1 wt%) micropillars at varied silicone oil temperature in the range of 30–130 °C. The length of the LCE, LCE/AuNR, and LCE/AuNS micropillars at varied temperatures for both thermal and photothermal actuation were determined and, respectively, summarized in **Figure 7**a–c. As noted previously (Figure 4) and also shown in Figure 7, the length change induced solely by thermal actuation in all three types of micropillars show very similar behavior. When the temperature is below ≈100 °C, the length change is minimal. In the transition range 100–120 °C, a drastic length reduction can be observed. With further increasing the temperature, the length reaches a constant value. With switching on the laser irradiation (photothermal actuation), the similar length–temperature behavior has been observed for all three types of pillars, but with noticeable down-shift of the transition region being observed for LCE/AuNR and LCE/AuNS pillars. The down-shift of the transition temperature in the photothermal actuation of LCE/AuNR and LCE/AuNS pillars suggests an additional temperature rise

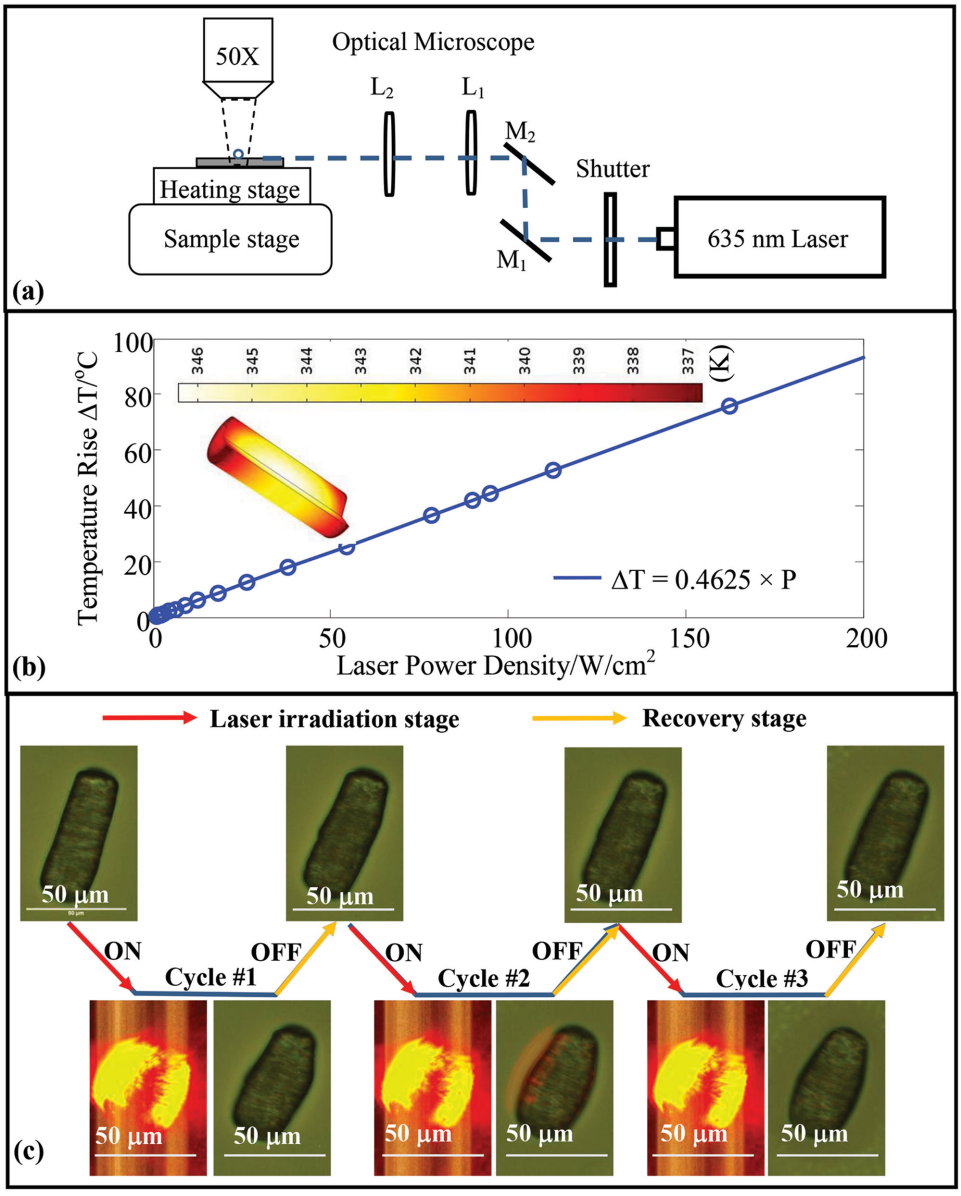

Figure 5. a) A schematic diagram of the experimental setup for real-time observing and recording the shape change of LCE/AuNP pillars under 635 nm high-power diode laser irradiation at various temperatures. L: focus lens; M: mirrors; b) finite elemental analysis (FEA) results on the temperature rise of a LCE/AuNR (1 wt%) micropillar (Length = 72.2 μm and Diameter = 24.6 μm) upon laser irradiation at varied power density. The inset shows the absolute temperature distribution (unit: Kelvin) of the pillar irradiated by 95 W cm^{-2} at an ambient temperature of 298.15 K. c) The snapshots of laser irradiation (95 W cm^{-2}) induced shape change for a LCE/AuNR (1 wt%) pillar at 80 °C. The cyclic shape change involves two stages: laser irradiation stage (laser on) and recovery stage (laser off).

is introduced due to the optical absorption of AuNP. By normalizing the pillar length to its value at 30 °C, the length–temperature data obtained in the photothermal and thermal actuation experiments can be superposed by up-shifting the temperature of the former a constant. This point can be clearly seen in **Figure 8**, where the amount of temperature shift for LCE, LCE/AuNR, and LCE/AuNS is, respectively, taken as 2, 48, and 12 °C. The superposition operation as shown in Figure 8 allows for a good estimate of the temperature rise induced by photothermal effect. In the case of LCE/AuNR (1 wt%), it is ≈48 °C and has a reasonable agreement with that determined by FEA analysis (44.2 °C, Table 1). For LCE/AuNS (1 wt%), such determined temperature rise due to laser irradiation is ≈12 °C; and it is lower than that calculated by the same FEA method (20.9 °C, Table 1). The higher temperature rise estimated by FEA in this case is due to that the absorption cross section at resonance condition (520 nm) was used in the calculation; and the photothermal actuation experiment was performed with a laser of 635 nm—an off-resonance condition. Both the FEA analysis and superposition results suggested that, at the same mass concentration (1 wt%), the temperature rise induced by photothermal effect in LCE/AuNR is higher than that in LCE/AuNS.

Table 1. Comparison of experimental and FEA results on the temperature rise of LCE/AuNR and LCE/AuNS micropillar under 95 W cm^{-2} 635 nm laser irradiation.

Pillar sample	FEA results (uniformheat source generation)		Experimental
	C_{abs}[a)] [cm^2 per Au-atom]	ΔT [°C]	ΔT [°C]
LCE/AuNR (1 wt%)	5.52×10^{-18}	44.2	48
LCE/AuNS (1 wt%)	2.27×10^{-18}	20.9	12
LCE/AuNR (0.5 wt%)	5.52×10^{-18}	24.9	43
LCE/AuNR (0.1 wt%)	5.52×10^{-18}	5.5	58

[a)]Optical absorption cross section of AuNP measured at the localized surface plasmon resonance wavelength 670 nm for AuNR and 520 nm for AuNS.

In other words, the AuNR is a better photothermal agent than AuNS, which makes the AuNR a much attractive candidate in developing photothermally actuated LCE actuators. The shape effect on the photothermal conversion of AuNP observed in our experiments is in line with the theoretical results. Within the framework of Rayleigh–Gans–Debye approximation and under equal volume/mass comparison,[49–51] the theoretically estimated optical absorption cross section at resonance condition for AuNR with diameter = 10 nm and length = 30 nm is about 5–6 times that of AuNS (diameter = 16.5 nm).

To study the effect of AuNR loadings, the LCE/AuNR microarrays with AuNR concentration of 0.1 and 0.5 wt% were prepared and their thermal and photothermal actuation behavior were investigated. **Figure 9** compares the length–temperature behavior obtained in the thermal and photothermal actuation experiments for LCE/AuNR micropillars with varied AuNR concentration (0.1, 0.5, and 1.0 wt%). As indicated by Figure 9, in the case of thermal actuation, the length–temperature behavior of the LCE/AuNR micropillars does not show significant dependence on the loadings of AuNR. The temperature range for the actuation transition is very similar for all three types of pillars. The onset temperature is located at ≈100 °C and the fully relaxed temperature occurs at ≈120 °C. It is noted that the 0.5 wt% pillar has a smaller maximum actuation strain (≈20%) as compared to 0.1 and 1 wt% sample (≈27%). As shown in Figure 9, the same trend of maximum actuation strain observed in thermal actuation (0.5 < 0.1 ≈ 1 wt%) reserves for the length–temperature behavior obtained in photothermal actuation experiments. We speculate that the variations of the mechanical and thermal mechanical properties of the LCE matrix induced by AuNR incorporation might play some roles responsible for this observation. Figure 9 indicates that all the pillars that were photothermally actuated show a down-shift of the actuation transition temperature when compared with the thermal actuation results. Certainly, the down-shift of the transition temperature is a result of the photothermal effect caused by the inclusion of AuNR. As shown by the FEA analysis (Table 1), when the mass concentration of AuNR is decreased from 1 to 0.1 wt%, the photothermal effect of AuNR and the corresponding temperature rise of the LCE/AuNR pillar would accordingly reduce. Under the same irradiation condition (95 W cm^{-2}), the temperature rise predicted by FEA analysis for 1, 0.5, and 0.1 wt% pillars is, respectively, 44.2, 24.9, and 5.5 °C. With the previously established superposition method (Figure 8), the experimentally observed temperature rise for 0.1 (58 °C) and 0.5 wt% (43 °C) LCE/AuNR micropillars in photothermal actuation was determined correspondingly and the results are listed in Table 1. Clearly, the lower is the AuNR concentration, the greater is the difference on the temperature rise given by the FEA analysis and the experimental observation.

The discrepancy between FEA modeling and the experimental observation is attributed to that the current simplified FEA model has not been able to completely capture the key physics of the photothermal actuation of LCE/AuNR micropillars. The simplified FEA model considered a uniform (constant) heat source density q induced by the laser irradiation, which has not truly reflected the real situation where the heat source density is position dependent. To make this point and understand the effect of nonuniform heating, we derived the heat source density distribution—$q(x, y)$ for a pillar with radius R and optical absorption coefficient α and under normal irradiation by a laser source with power density of P_0. It is written as

$$q(x,y) = \alpha P_0 \exp\left[-\alpha\left(\sqrt{R^2 - y^2} - x\right)\right] \quad (1)$$

The derivation details for Equation (1) can be found in the Supporting Information. With Equation (1), the heat source distribution for a pillar of diameter 24.6 μm irradiated with 95 W cm^{-2} at varied optical absorption coefficients were calculated. **Figure 10**a and Figure S7a, Supporting Information, show a few representative examples, where one can visualize that, in the region of the pillar facing toward the laser source, the heat source density is higher; and in the opposite side, the heat source density is lower. The gradient of heat source density increases with the absorption coefficient. The nonuniformly distributed heat source density would induce a nonuniform temperature distribution across the entire volume of the pillar. As a consequence, for a given irradiation condition, some region of the pillar may have a temperature lower than the transition temperature and cannot be

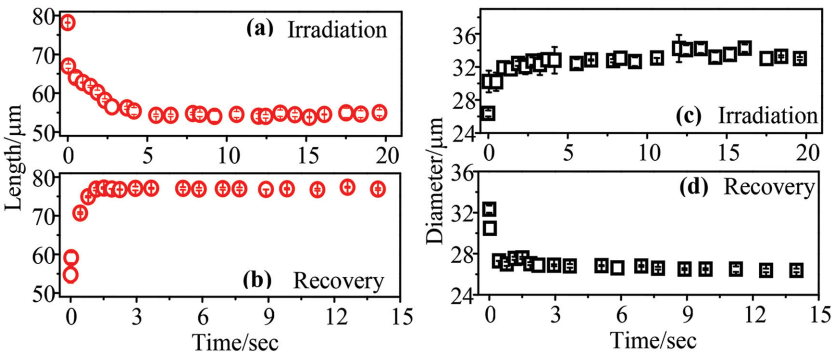

Figure 6. Photothermal actuation induced time-dependent length and diameter change for LCE/AuNR (1 wt%) micropillar immersed in silicone oil at 80 °C. a) Length change in irradiation stage (laser ON); b) length change in recovery stage (laser OFF); c) diameter change in irradiation stage (laser ON); d) diameter change in recovery stage (laser OFF).

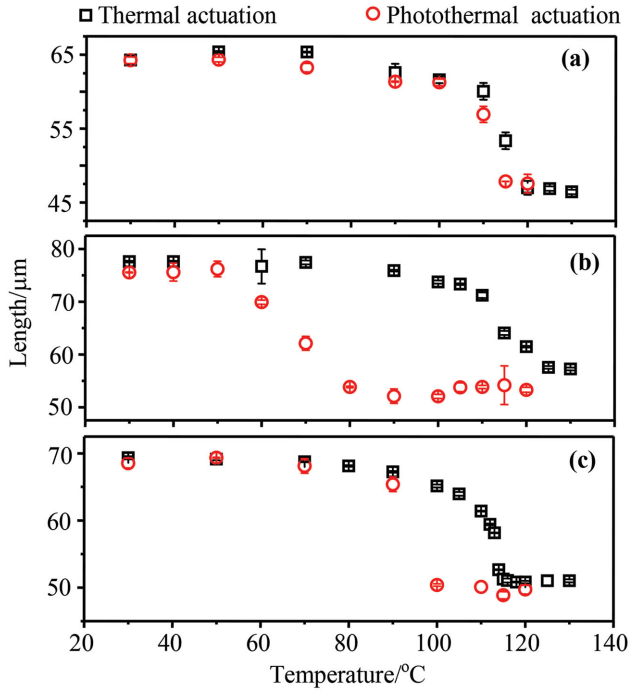

Figure 7. Comparison of the thermal actuation and photothermal actuation on the length change of a) LCE, b) LCE/AuNR (1 wt%), and c) LCE/AuNS (1 wt%) micropillars at varied temperatures.

actuated. Let q_{th} be a threshold heat source density. If $q(x, y)$ is smaller than q_{th}, there is no actuation occurred at the position (x, y). Then we can define a volume-fraction-of-actuation (VFA), which is the fraction of the pillar volume with $q(x, y)$ greater than q_{th}. Apparently, a large VFA is desired for a pillar to have better photothermal actuation response. By setting $q_{th} = 1.5 \times 10^4$ W cm^{-3}—a value that would result in a temperature

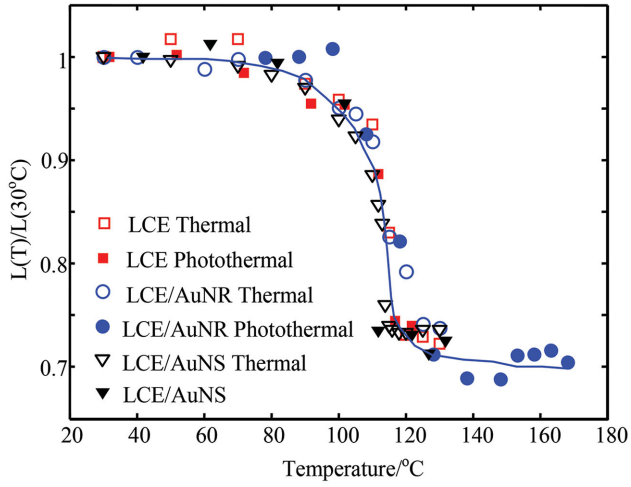

Figure 8. Superposition of the length–temperature behavior for LCE, LCE/AuNR (1 wt%), and LCE/AuNS (1 wt%) micropillars under thermal and photothermal actuation. To create the superposition plot, the photothermal actuation data shown in Figure 7 are up-shifted against the corresponding thermal actuation data by 2 °C for LCE, 12 °C for LCE/AuNS, and 48 °C for LCE/AuNR.

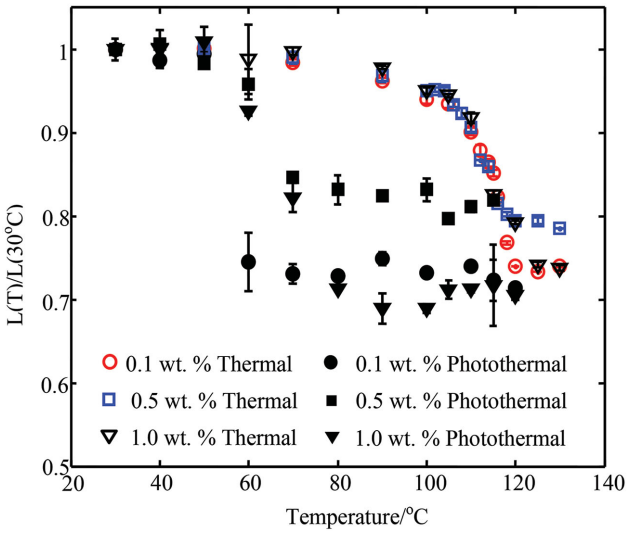

Figure 9. Comparison of the length–temperature behavior of LCE/AuNR micropillars with varied AuNR mass loadings under thermal and photothermal actuation.

rise of $\Delta T = 35$ °C when uniform heating is considered—we evaluated the VFA for the pillar with a diameter of 24.6 μm under 95 W cm^{-2} irradiation at varied optical absorption coefficients, α. The 2D visualization of such results is shown in Figure 10b and Figure S7b, Supporting Information; and the effect of α on VFA at different q_{th} is summarized in Figure 10c. The results shown in Figure 10c suggest that there exists a best value or a range of best values of α to optimize VFA. When away from the optimum condition, the same value of VFA can be achieved through formulating a micropillar with either a low α or a high α. Besides VFA, the averaged heat source density q_{avg} is also considered an important quantity in understanding the photothermal actuation behavior of LCE/AuNR micropillars. Upon integrating Equation (1) over the pillar volume, one can easily obtain the expression of q_{avg} for the nonuniform heating case (Equation (S5), Supporting Information). With the same pillar considered previously, we have evaluated the effect of optical absorption coefficient α on q_{avg}. The result is shown in Figure 10d. Evidently, the photothermal conversion does not monotonically increase with increasing the optical absorption of the micropillar. There is a saturation on q_{avg} when α exceeds ≈1000 cm^{-1}. This result along with the previously introduced VFA concept suggests that the dependence of the photothermal actuation transition for a LCE/AuNR micropillar on its optical absorption coefficient is a complicated issue. We consider two simple scenarios here. In one scenario, a pillar with a high α is in the saturation regime and another with a low α is not. Both of them have a similar VFA. In another scenario, both pillars are in the saturation regime and the one with smaller α has a larger VFA. In these two scenarios, we expect the pillar with low α could show similar photothermal actuation response as the one with high α or even better. The complicated problem mentioned above can be even more involved when considering that the optical absorption of LCE/AuNR and the associated photothermal effect depends on not only the concentration of AuNRs but

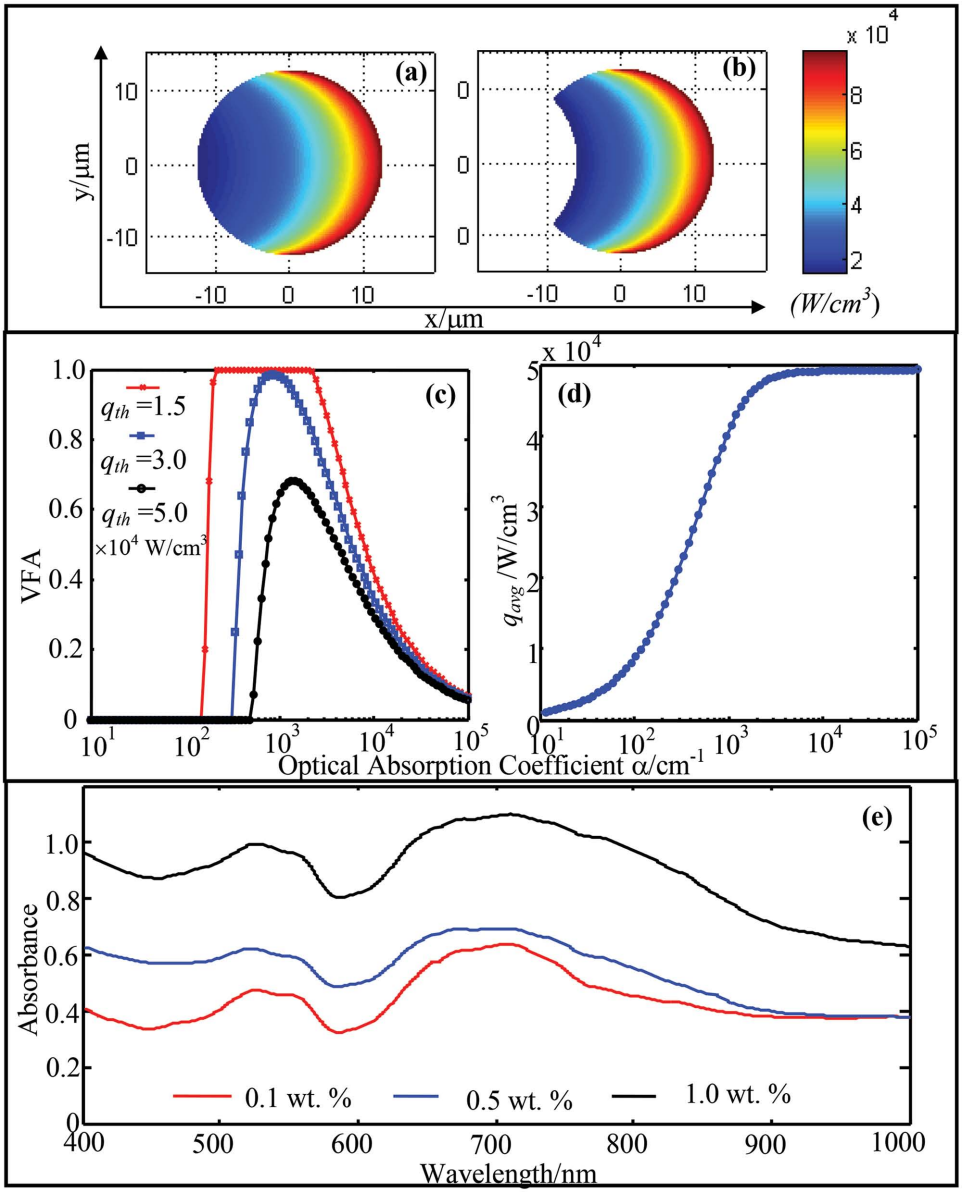

Figure 10. a) Heat source density distribution $q(x, y)$ for a pillar with diameter 24.6 μm and optical absorption coefficient of 1000 cm^{-1} normally irradiated by a laser power density 95 W cm^{-2}. b) The same result as (a) but with $q(x, y) \geq q_{th} = 1.5 \times 10^4$ W cm^{-3} shown for a visualization of the volume-fraction-of-actuation (VFA). c) Effect of optical absorption on VFA at different threshold heat source density values. When the pillar is uniformly heated with $q_{th} = 1.5$, 3.0, and 5.0×10^4 W cm^{-3}, the corresponding temperature rise is, respectively, $\Delta T = 35$, 70, and 116 °C. d) Effect of optical absorption on the volume-average heat source density q_{avg}. e) Comparison of the UV–vis–NIR spectra of LCE/AuNR composite films with varied gold concentrations.

also their aggregated structures. Figure 10e compares the UV–vis-NIR absorption spectra of LCE/AuNR thin films with gold loading of 0.1, 0.5, and 1.0 wt%. The presence of AuNR aggregates in all samples is clearly indicated by the broadened LSPR bands, albeit with 0.1 wt% sample showing a less degree of broadening effect. Due to an intensively studied plasmon coupling phenomenon,[52] the assembly/aggregate of AuNR nanoparticles can possess the enhanced photothermal conversion effect.[53,54] However, if the size of aggregates is too large, e.g., at high loadings of gold nanoparticles, the enhanced photothermal effect would be deteriorated, since the particles in the interior of the aggregates cannot be accessed by the incident light field due to the screening of the exterior particles. The arguments made above regarding the nonuniform heat source density distribution and aggregation structure dependent photothermal conversion effect clearly suggest that a multiphysics approach is necessary in order to fully understand the photothermal actuation behavior of LCE/AuNR micropillars. It involves light/AuNR and light/AuNR aggregates interaction, the associated enhanced/deteriorated photothermal conversion effect, and the interplay between the volume-fraction-of-actuation and the mechanical and thermomechanical properties of the LCE/AuNR micropillars. It is not an easy task and should be considered a separate research topic.

3. Conclusions

A novel experimental protocol was developed to enable successful incorporation of gold nanosphere and nanorod (AuNS and AnNR) into polyacrylate-based liquid crystal elastomer for fabricating LCE/AuNR and LCE/AuNS micropillars and microactuators. With a mass loading less than 1 wt%, the AuNR- and AuNS-enabled LCE micropillars show the same excellent thermal actuation ability as the neat LCE pillars. Moreover, the surface plasmon resonance enhanced optical absorption of AuNP allows a new way to photothermally actuate the shape change of LCE/AuNP micropillar upon visible laser irradiation. The LCE/AuNR micropillar possesses a rapid response time and meanwhile is able to maintain very high maximum actuation strain. In contrast to the thermally actuated LCE, the LCE/AuNP microactuator with photothermal actuation capability can be precisely targeted by manipulating the laser beam to induce the actuation movement without perturbing the surrounding environment.

4. Experimental Section

Preparation of the LCE Monomer: The LCE monomer 4″-acryloyloxybutyl 2,5-di(4′-butyloxybenzoyloxy) benzoate (4-ADBB) was prepared through a three-step reaction according to the procedure disclosed in ref. [13].

Synthesis and Characterization of Gold Nanoparticles: Gold nanoparticles were synthesized according to the seed-mediated growth method developed by El-Sayed and Nikoobakht.[45] In brief, the seed solution was prepared by first mixing the aqueous solution of cetyltrimethyl ammonium bromide (CTAB, 5 mL, 0.10 M) with tetrachlorauric acid solution ($HAuCl_4$, 25 µL, 50×10^{-3} M). To this mixture, a freshly prepared ice-cold sodium borohydride solution ($NaBH_4$, 300 µL, 10×10^{-3} M) was subsequently added. Upon a continued mild stirring for 30 s, the seed solution turned into tea-like color. It was then kept quiescent at 25 °C for at least 2 h before use. The growth solution was prepared first by adding an aqueous solution of ascorbic acid (75 µL, 100×10^{-3} M) to a freshly prepared mixture of $HAuCl_4$ (100 µL, 50×10^{-3} M) and CTAB (10 mL, 0.10×10^{-3} M). With addition of ascorbic acid, the mixture turned from yellowish to colorless. Subsequent to the color change, either no or 150 µL silver nitrate ($AgNO_3$, 5×10^{-3} M) was added for size and shape control of the gold nanoparticles.[45] The former case resulted in AuNS; and the latter case resulted in AuNR. To this freshly prepared growth solution, a 60 µL seed solution aged for 2 h was then added with vigorously stirring. While maintained at 28 °C, this mixed solution was continually stirred mildly for over 24 h to result in a AuNR aqueous dispersion of dark purple color or a AuNS aqueous dispersion in pink color. An Agilent 8453 UV–vis-NIR spectrophotometer and a Hitachi HT7700 were, respectively, used to acquire the UV–vis-NIR spectra and TEM images of the as-synthesized gold nanoparticles (AuNS and AuNR) to confirm their successful formation.

Preparation and Characterization of AuNR/AuNS Included LCE Monomer: The gold nanoparticle aqueous dispersion prepared previously (both AuNS and AuNR) was centrifuged at 12 000 rpm for 15 min by using a Hitachi Himac CR22g supercentrifuge. Followed by centrifugation, the supernatant was discarded and the precipitate was redispersed in warm water, which was then centrifuged with the same condition (12000 rpm, 15 min). This procedure was repeated several times to remove the excess CTAB. After the repeated centrifugation process, an appropriate amount of gold nanoparticles was dispersed in the solution of 4-ADBB in tetrahydrofuran (THF) under sonication. Followed by THF evaporation and drying, the mixture of 4-ADBB monomer with AuNR/AuNS was obtained for later use in fabricating LCE/AuNR or LCE/AuNS composite pillars. An Agilent 8453 UV–vis-NIR spectrophotometer was used to acquire the UV–vis-NIR spectra of the dispersion of AuNR/4-ADBB and AuNS/4-ADBB in THF to confirm the successful incorporation of gold nanoparticles into LCE monomers.

Fabrication and Characterization of LCE, LCE/AuNR, and LCE/AuNS Composite Films and Micropillars: According to the previously reported procedures,[11,13,39] a PDMS mold with an array of holes of diameter of 20 µm was used to fabricate LCE, LCE/AuNR, and LCE/AuNS micropillar arrays. In brief, the monomer of LCE or LCE included with gold nanoparticles was first mixed with crosslinking agent 1, 6-hexanediol diacrylate and photoinitiator 2-benzyl-2-(dimethylamino)-4′-morpholinobutyrophenone in THF at a molar ratio of 77:18:5. Upon evaporation of THF and drying, a small amount of the dried mixture of 4-ADBB/crosslinking agent/photoinitiator or 4-ADBB/gold nanoparticles/crosslinking agent/photoinitiator was placed on a piece of cover glass that was supported by a permanent magnet (1 T NdFeB rare earth magnet). The entire assembly was then heated to 100 °C to melt the mixtures. Subsequently, the PDMS mold was brought in contact with the melt. This state was maintained at 100 °C for ≈10 min to allow for a complete filling of the mold holes. After the filling process, the temperature was reduced to 55 °C at a cooling rate of 1 °C min^{-1} to allow for the transition of the monomer mixture from isotropic to nematic phase. While maintaining the temperature at 55 °C for additional 10 min and under argon protection, UV irradiation (high pressure mercury lamp, 300 mW cm^{-2}) was applied for 2 h to photopolymerize/photocrosslink the monomer mixture. At the end of crosslinking process, the entire assembly was cooled to room temperature to release the PDMS mold from the glass slide for forming LCE, LCE/AuNR, or LCE/AuNS micropillar arrays. The isolated micropillars used for thermal actuation and photothermal actuation study were manually cut from the micropillar array with a blade. The LCE, LCE/AuNR, and LCE/AuNS sample prepared above were subjected to DSC test to examine the effect of gold nanoparticles on the phase transition temperature of the LCE host. TGA was performed to confirm the mass concentration of gold nanoparticles in the prepared LCE/AuNR and LCE/AuNS composite samples. Both DSC and TGA test were carried out on a DSC Q2000 system under nitrogen atmosphere at a heating rate of 10 °C min^{-1}. The UV–vis-NIR spectra for thin film samples of LCE, LCE/AuNR, and LCE/AuNS deposited on a glass substrate were acquired by an Agilent 8453 UV–vis-NIR spectrophotometer to examine the dispersion states of gold nanoparticles. The spectrum of LCE sample was taken with air as the reference; and the spectra for composite thin films were taken with the LCE thin film as the reference. For the same purpose, Hitachi HT7700 was applied to acquire TEM images of the ultrathin sections of LCE/AuNR and LCE/AuNS composites. For each sample, the ultrathin section of 100 nm in thickness was prepared by a Leica EM UC6 ultramicrotome. Simultaneous microfocused WAXS and SAXS measurements were performed on a Bruker NanoSTAR system equipped with a microfocus x-ray source (IµS, Incoatec GmbH, Geesthacht, Germany) operating at 45 kV and 650 mA with wavelength of Cu K$\alpha\lambda$ = 0.1542 nm. The three-pinhole system was set at the size of 750, 400, and 1000 µm for collecting both WAXS and SAXS patterns. The WAXS pattern was recorded and scanned, respectively, by a Fuji Photo Film image plate and Fuji FLA-7000 scanner. The SAXS pattern was recorded by a 2D multiwire Hi-STAR detector. In WAXS, the sample to detector distance was 5.2 cm; and in SAXS, the sample to detector distance was 104.3 cm. In both WAXS and SAXS measurements, a 2 h exposure time was used to collect the WAXS and SAXS patterns for LCE, LCE-AuNS, and LCE-AuNR micropillar arrays.

Photo- and Thermal Actuation of LCE, LCE/AuNR, and LCE/AuNS Pillars: A Nikon LV 1000 POL microscope equipped with a Nikon DS-fi2 CCD camera was used to capture the optical images and videos of the LCE, LCE/AuNR, and LCE/AuNS micropillars to visualize and quantify their actuation behaviors. For thermal actuation scheme, the isolated pillars were suspended in methylsilicone oil 201 (J&K Chemical Ltd., China) supported by a piece of cover glass, the temperature of which was controlled by a computer-controlled Linkam CSS450 hot stage. The same microscopy setup was used to visualize and record the photothermal actuation of LCE/AuNR and LCE/AuNS micropillars, which was performed with a diode laser of 635 nm (Changchun New Industries Optoelectronics Tech, CO., Ltd., nominal power of 5 W). Figure 5a

schematically shows the inhouse assembled optics used for this experiment. After reflection mirrors and beam shaping lenses, the power density of the laser beam received by the pillar samples was measured to be 95 W cm^{-2}. A photograph of the optical setup and the related details on the determination of the laser power density can be found in Figure S3a,b, Supporting Information. For each type of micropillar arrays (LCE, LCE/AuNR—0.1, 0.5, 1.0 wt% and LCE-AuNS—1.0 wt%), an isolated pillars were randomly selected and used for investigating their thermal and photothermal actuation induced size change. The acquired pillar image at a given actuation setting was measured three times for estimating the measurement variations on the length and diameter of the micropillar. Unless stated otherwise, the error-bar associated with the actuation results is one standard deviation to reflect such a measurement variation. To examine the sample-to-sample variation, two LCE/AuNR (1 wt%) microarray samples (Sample1 and Sample2) were separately prepared and tested for their thermal and photothermal actuation behavior. Figure S5, Supporting Information, compares the results.

Supporting Information

Supporting Information is available from the Wiley Online Library or from the author.

Acknowledgements

The financial support from the NSFC under Project Nos. 51233002 and 51061130556 is gratefully acknowledged. T. Liu would like to acknowledge Tsinghua Global Scholars Fellowship for the sponsorship and Key Laboratory of Advanced Materials, Department of Chemical Engineering, Tsinghua University, for the kind host to perform this work. P. Keller would like to acknowledge the support from the French ANR (Project No. ANR-10-INTB-0904) and the NSF (Grant No. DMR-0213918).

Received: February 2, 2015
Revised: March 14, 2015
Published online: April 9, 2015

[1] F. Brommel, D. Kramer, H. Finkelmann, *Adv. Polym. Sci.* **2012**, *250*, 1.
[2] A. Lebar, G. Cordoyiannis, Z. Kutnjak, B. Zalar, *Adv. Polym. Sci.* **2012**, *250*, 147.
[3] W. H. de Jeu, B. I. Ostrovskii, *Adv. Polym. Sci.* **2012**, *250*, 187.
[4] M. Warner, E. M. Terentjev, *Liquid Crystal Elastomers*, 2nd Ed., Oxford University Press, Oxford **2003**.
[5] C. Ohm, M. Brehmer, R. Zentel, *Adv. Polym. Sci.* **2012**, *250*, 49.
[6] T. Mirfakhrai, J. D. W. Madden, R. H. Baughman, *Mater Today* **2007**, *10*, 30.
[7] I. A. Anderson, T. A. Gisby, T. G. McKay, B. M. O'Brien, E. P. Calius, *J. Appl. Phys.* **2012**, *112*, 041101
[8] C. Ohm, M. Brehmer, R. Zentel, *Adv. Mater.* **2010**, *22*, 3366.
[9] C. L. van Oosten, C. W. M. Bastiaansen, D. J. Broer, *Nat. Mater.* **2009**, *8*, 677.
[10] M. Yamada, M. Kondo, J. Mamiya, Y. Yu, M. Kinoshita, C. J. Barrett, T. Ikeda, *Angew. Chem. Int. Ed.* **2008**, *120*, 5064.
[11] H. Yang, A. Buguin, J.-M. Taulemesse, K. Kaneko, S. Mery, A. Bergeret, P. Keller, *J. Am. Chem. Soc.* **2009**, *131*, 15000.
[12] A. L. Elias, K. D. Harris, C. W. M. Bastiaansen, D. J. Broer, M. J. Brett, *J. Mater. Chem.* **2006**, *16*, 2903.
[13] R. Wei, L. Zhou, Y. He, X. Wang, P. Keller, *Polymer* **2013**, *54*, 5321.
[14] C. M. Spillmann, J. Naciri, B. D. Martin, W. Farahat, H. Herr, B. R. Ratna, *Sens. Actuators A* **2007**, *133*, 500.
[15] H. Finkelmann, E. Nishikawa, G. G. Pereira, M. Warner, *Phys. Rev. Lett.* **2001**, *87*, 015501.
[16] Y. Yu, M. Nakano, T. Ikeda, *Nature (London)* **2003**, *425*, 145.
[17] M. Chambers, H. Finkelmann, M. Remskar, A. Sanchez-Ferrer, B. Zalar, S. Zumer, *J. Mater. Chem.* **2009**, *19*, 1524.
[18] L. Yang, K. Setyowati, A. Li, S. Gong, J. Chen, *Adv. Mater.* **2008**, *20*, 2271.
[19] R. R. Kohlmeyer, J. Chen, *Angew. Chem. Int. Ed.* **2013**, *52*, 9234.
[20] A. Kaiser, M. Winkler, S. Krause, H. Finkelmann, A. M. Schmidt, *J. Mater. Chem.* **2009**, *19*, 538.
[21] Y. Sun, J. S. Evans, T. Lee, B. Senyuk, P. Keller, S. He, I. I. Smalyukh, *Appl. Phys. Lett.* **2012**, *100*, 241901.
[22] R. Montazamia, C. M. Spillmann, J. Naciri, B. R. Ratna, *Sens. Actuators A* **2012**, *178*, 175.
[23] K. A. Willets, R. P. Van Duyne, *Annu. Rev. Phys. Chem.* **2007**, *58*, 267.
[24] W. A. Murray, W. L. Barnes, *Adv. Mater.* **2007**, *19*, 3771.
[25] L. Cao, D. N. Barsic, A. R. Guichard, M. L. Brongersma, *Nano Lett.* **2007**, *7*, 3523.
[26] S. Link, Z. L. Wang, M. A. El-Sayed, *J. Phys. Chem. B* **2000**, *104*, 7867.
[27] S. Link, C. Burda, M. B. Mohamed, B. Nikoobakht, M. A. El-Sayed, *J. Phys. Chem. A* **1999**, *103*, 1165.
[28] X. Huang, I. H. El-Sayed, W. Qian, M. A. El-Sayed, *J. Am. Chem. Soc.* **2006**, *128*, 2115.
[29] X. Liu, M. Atwater, J. Wang, Q. Huo, *Colloids Surf. B* **2007**, *58*, 3.
[30] C. J. Orendorff, C. J. Murphy, *J. Phys. Chem. B* **2006**, *110*, 3990.
[31] T. Liu, Z. Xiao, B. Wang, *Carbon* **2009**, *47*, 3529.
[32] M. F. Islam, D. E. Milkie, C. L. Kane, A. G. Yodh, J. M. Kikkawa, *Phys. Rev. Lett.* **2004**, *93*, 037404.
[33] Y. Murakami, E. Einarsson, T. Edamura, S. Maruyama, *Phys. Rev. Lett.* **2005**, *94*, 087402.
[34] S. Link, M. B. Mohamed, M. A. El-Sayed, *J. Phys. Chem. B* **1999**, *103*, 3073.
[35] J. Perez-Juste, I. Pastoriza-Santos, L. M. Liz-Marzan, P. Mulvaney, *Coord. Chem. Rev.* **2005**, *249*, 1870.
[36] H. H. Richardson, M. T. Carlson, R. J. Tandler, P. Hernandez, A. O. Govorov, *Nano Lett.* **2009**, *9*, 1139.
[37] K. Jiang, D. A. Smith, A. Pinchuk, *J. Phys. Chem. C* **2013**, *117*, 27073.
[38] Z. Xiao, Q. Wu, S. Luo, C. Zhang, J. Baur, R. Justice, T. Liu, *Part. Part. Syst. Charact.* **2013**, *30*, 338.
[39] A. Buguin, M.-H. Li, P. Silberzan, B. Ladoux, P. Keller, *J. Am. Chem. Soc.* **2006**, *128*, 1088.
[40] H. Yang, G. Ye, X. Wang, P. Keller, *Soft Matter* **2011**, *7*, 815.
[41] Z. Q. Yang, G. A. Herd, S. M. Clarke, A. R. Tajbakhsh, E. M. Terentjev, W. T. S. Huck, *J. Am. Chem. Soc.* **2006**, *128*, 1074.
[42] C. Ohm, C. Serra, R. Zentel, *Adv. Mater.* **2009**, *21*, 4859.
[43] S. Haseloh, C. Ohm, F. Smallwood, R. Zentel, *Macromol. Rapid Commun.* **2011**, *32*, 88.
[44] C. Ohm, N. Haberkorn, P. Theato, R. Zentel, *Small* **2011**, *7*, 194.
[45] B. Nikoobakht, M. A. El-Sayed, *Chem. Mater.* **2003**, *15*, 1957.
[46] Q. Liu, Y. Cu, D. Gardner, X. Li, S. He, I. I. Smalyukh, *Nano Lett.* **2010**, *10*, 1347.
[47] Shin-Etsu Silicone, Silicone Fluid KF-96 performance Test results, http://www.silicone.jp/e/catalog/pdf/kf96_e.pdf (accessed: December **2014**).
[48] S. W. Churchill, H. H. Chu, *Int. J. Heat Mass Transfer* **1975**, *18*, 1323.
[49] G. V. Hartland, *Annu. Rev. Phys. Chem.* **2006**, *57*, 403.
[50] S. Link, M. B. Mohamed, M. A. El-Sayed, *J. Phys. Chem. B* **1999**, *103*, 3073.
[51] S. W. Prescott, P. Mulvaney, *J. Appl. Phys.* **2006**, *99*, 123504.
[52] N. G. Khlebtsov, L. A. Dykman, *J. Quant. Spectrosc. Radiat. Transfer* **2010**, *111*, 1.
[53] G. Baffou, C. Girard, R. Quidant, *Phys. Rev. Lett.* **2010**, *104*, 136805.
[54] M. A. Mackey, M. R. K. Ali, L. A. Austin, R. D. Near, M. A. El-Sayed, *J. Phys. Chem. B* **2014**, *118*, 1319.